Polychromatic Maximum Likelihood Reconstruction for Talbot-Lau X-ray Tomography

Florian Schiffers[*†], Sebastian Kaeppler[†], Georg Pelzer[*], Andreas Wolf[*],
Andreas Maier[†], Gisela Anton[*], Christian Riess[†]

[*]Erlangen Centre for Astroparticle Physics,
Friedrich-Alexander-University of Erlangen-Nuremberg, Erlangen, Germany
[†]Pattern Recognition Lab, Department of Computer Science,
Friedrich-Alexander-University of Erlangen-Nuremberg, Erlangen, Germany

Abstract—Compared to conventional attenuation imaging, Talbot-Lau X-ray grating interferometry applied within a polychromatic setup suffers from additional artifacts. Among those are beam hardening and dispersion effects due to the complex coupling of different physical effects involved in the image formation process. In computed tomography these effects lead to image degradation, such as cupping and streak artifacts, hampering diagnostic use.

In this paper, we seek to reduce these artifacts in an iterative reconstruction framework. To this purpose, we define a model of the polychromatic forward projection that includes prior knowledge about the physical setup. Using this model we derive a maximum likelihood algorithm for simultaneous reconstruction of the attenuation, phase and scatter images.

In our experiments on a synthetic ground-truth phantom, we compare filtered backprojection reconstruction with the proposed approach. The proposed method considerably reduces strong beam hardening artifacts in the phase images, and almost completely removes these artifacts in the absorption and scatter images.

Index Terms—X-ray interferometry, Talbot-Lau, beam hardening, iterative reconstruction

I. Introduction

Over the last decades a great effort was made to understand imaging modalities exploiting the wave properties of X-rays [1]–[3]. Among those is Talbot-Lau grating-based phase-contrast X-ray imaging, which allows for simultaneous measurement of attenuation, the phase shift that occurs while traversing the material, and the specimen's small-angle scattering properties. Beneficial contrast for medical application was reported for the differential phase-contrast signal when differences in soft-tissue are of importance [4], [5]. Additionally, the dark field contrast yields complementary information if the specimen provides highly varying structures on the small scale, such as lung tissue [6], [7] or porous media like calcification in mammography [8], [9]. The technique offers great prospects for future clinical applications, since the setup has proven to work well when embedded in a conventional X-ray absorption setup [10], [11].

However, tomographic reconstructions of data from a polychromatic setup suffer from artifacts due to two energy-dependent factors. The first factor are the energy-dependent material coefficients [12]–[15], an issue which is the analog to conventional attenuation X-ray. For attenuation X-ray, this is
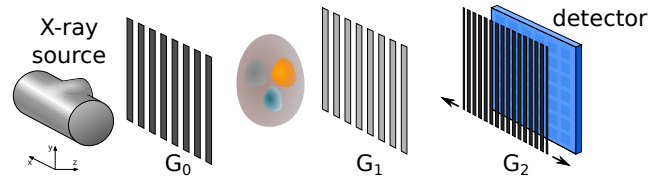
Fig. 1: Sketch of a typical Talbot-Lau interferometer.

a long-standing, much-researched problem [16]–[18]. The second factor that is specific to Talbot-Lau interferometers is the energy-dependence of the interferometer visibility. This leads to beam hardening and dispersion effects in both phase [12], [13] and dark-field signals [14], [19]. We will address both factors in the proposed method to reduce polychromatic artifacts.

Bevins *et al.* and Chabior *et al.* presented first experimental evidence of beam hardening in phase-contrast tomography [12], [13]. Chabior *et al.* and Koehler *et al.* adapted linearization techniques known from conventional CT [20] to Talbot-Lau imaging [13], [21], but performed no evaluation on tomographic data. We are unaware of any beam-hardening correction that is specifically tailored to Talbot-Lau interferometers.

For tomographic reconstruction of Talbot-Lau data, Brendel *et al.* and Ritter *et al.* investigated a maximum-likelihood algorithm to simultaneously reconstruct attenuation, phase and scatter images without requiring phase retrieval [22]–[24]. This method can not cope with polychromatic data, because a monochromatic source was used to model the forward projection.

Our key contribution is to extend the monochromatic forward model [23], [24] to polychromatic data. The main benefit of the extended model is that beam-hardening artifacts are implicitly dampened or even completely removed. We show how prior knowledge can be used to approximate the energy dependence of materials. Furthermore, we use this model to propose an iterative reconstruction algorithm for polychromatic CT based on maximum-likelihood techniques [25]. To our knowledge, this is the first work that addresses polychromaticity-induced artifacts in an iterative reconstruction framework for
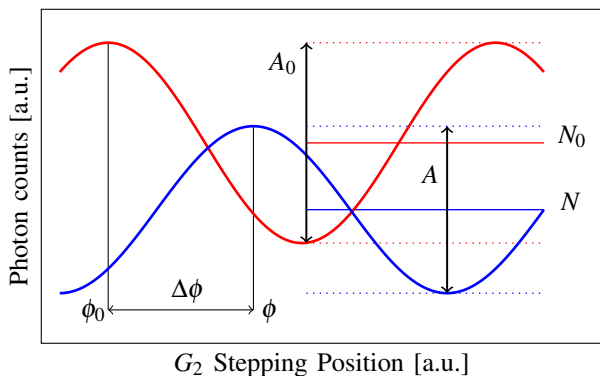
Fig. 2: Red: Reference stepping curve without object, Blue: Object stepping curve. Each curve is described by three parameters: The offset N, the phase ϕ, and amplitude A. The visibility is then given by $V := \frac{A}{N}$.

Talbot-Lau imaging.

We validate the reconstruction algorithm with synthetic projection data of a well-defined phantom. The data reconstructed by the proposed algorithm are compared to results obtained through standard filtered backprojection techniques, achieving a considerable reduction of beam-hardening artifacts.

II. METHODS

We first briefly review the grating-based Talbot-Lau X-ray interferometer in Sec. II-A. An energy-dependent, yet tractable physical model is presented in Sec. II-B. The associated reconstruction algorithm is presented in II-C.

A. Talbot-Lau Grating Interferometer

A Talbot-Lau grating interferometer, shown in Fig. 1, consists of a standard X-ray tube and a detector, and three gratings G_0, G_1, G_2 between source and detector. The source grating G_0 ensures spatial coherence. The phase grating G_1 imprints a periodic phase offset onto the wave front. At a distance downstream of G_1, this periodic offset leads to the Talbot effect [26]. The resulting interference pattern is sampled by stepping the analyzer grating G_2.

The stepping data allow to compute three quantities, namely the mean photon count N, the phase ϕ, and the overall setup visibility V, see Fig. 2. In a polychromatic setup, the observed N, ϕ and V are integrated over all wavelengths of the energy spectrum. To obtain absorption, differential phase and dark-field of a specimen, the images are normalized with reference acquisitions N_0, ϕ_0, V_0. These reference images are recorded from an additional free-field scan.

B. A Physical Model with Energy Dependence

The physical model needs to be carefully chosen. On one hand, a more expressive model allows a more accurate physical interpretation of the data. On the other hand, the model has to remain manageable for the reconstruction algorithm to achieve convergence. The proposed model presents a tradeoff between these two aspects.

The desired result of tomographic reconstruction is the material distribution of a specimen. In the case of Talbot-Lau tomography, this material distribution has to be inferred from attenuation, refractive decrement and scattering properties. To allow for the avoidance of beam-hardening artifacts, we define the measured quantities in dependence of the energy.

As a starting point, we review established models for absorption, phase, and scatter per energy for a Talbot-Lau interferometer [12], [13], [27]. In the energy range between $E = 5\,\mathrm{keV}$ to $E = 120\,\mathrm{keV}$, the energy-dependent linear attenuation coefficient $\mu(E)$ can be approximately decomposed into the photoelectric cross-section and the Compton scatter,

$$\mu(E) = \rho_e \cdot \left(C_1 \frac{Z^{C_2}}{E^3} + \sigma_{kn}(E) \right) \; , \tag{1}$$

where ρ_e is the electron density, σ_{kn} is the Klein-Nishina approximation for the differential cross-section of scattered photons. C_1 is a scalar that depends on natural constants. C_2 is a scalar that varies only slowly with energy, such that it can be approximated as $C_2 \approx 3$ [27]. Equation 1 assumes no K-edge effects, which is valid for biological tissue in the energy range of interest.

The phase shift $\phi(E)$ of an X-ray with energy E propagating through matter is given by the integral along the line of sight l,

$$\phi(E) = \frac{r_e hc}{E} \int_l \rho_e(l)\, \mathrm{d}l \; , \tag{2}$$

where r_e denotes the electron radius, h Planck's constant, and c speed of light. Talbot-Lau interferometry does not measure $\phi(E)$ directly. Instead, it measures the refraction angle $\alpha(E)$ proportional to the gradient of the phase-shift, i.e.,

$$\alpha(E) = \frac{hc}{2\pi E} \frac{\partial}{\partial x} \phi = \frac{\partial}{\partial x} \int_l \delta(E)\, \mathrm{d}l \; , \tag{3}$$

with the refractive element $\delta(E)$ given by

$$\delta(E) = \frac{h^2 c^2 r_e}{2\pi} \frac{\rho_e}{E^2} \; . \tag{4}$$

To our knowledge, there exists no full theoretical model for the energy-dependence of the scatter coefficient σ. Following the work by Bech *et al.* [6], we model the scatter coefficient analogously to the attenuation coefficient.

However, it turns out that a full model in the sense of Eqn. 1 and Eqn. 4 is challenging to reconstruct. Thus, to keep the model manageable, energy dependence is approximated using monomials for each coefficient μ, δ, σ by defining

$$\mu(E) = \mu(E_0) \cdot \left(\frac{E}{E_0} \right)^{C_\mu} \; , \tag{5}$$

$$\delta(E) = \delta(E_0) \cdot \left(\frac{E}{E_0} \right)^{C_\delta} \; , \tag{6}$$

$$\sigma(E) = \sigma(E_0) \cdot \left(\frac{E}{E_0} \right)^{C_\sigma} \; . \tag{7}$$
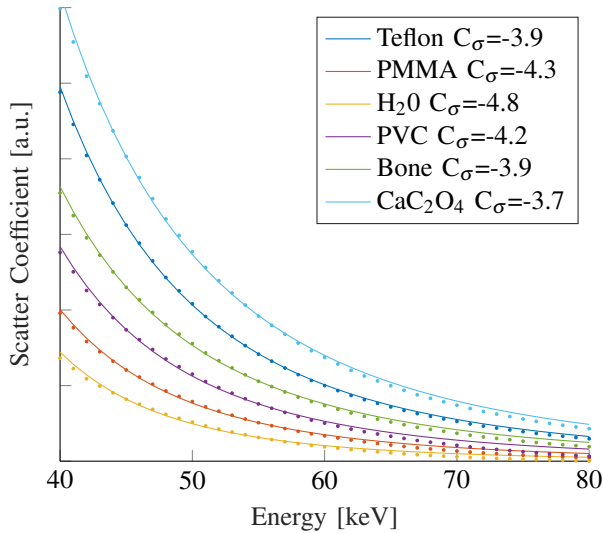
Fig. 3: Simulation results for the scatter coefficient of different materials.

Fig. 4: Footprint of the Kaiser-Bessel functions.

Here, the material coefficients $\mu(E_0), \delta(E_0), \sigma(E_0)$ are assumed to be known at a given energy E_0 and then extrapolated to arbitrary energies E. The exponents are set to $C_\mu = -3$, $C_\delta = -2$ according to physical properties described in Eqns. (1) and (4). Doing so, we considered only the first term in Eqn. (1) and omitted the energy-dependence of the Klein-Nishina approximation.

The energy dependence of the scatter coefficient is not yet fully explored. While attenuation and phase-sensitive imaging can be explained by material properties, the linear scatter coefficient also depends on the actual setup parameters. We use the wave propagation algorithm of [14], [28] to simulate the scatter coefficient at different energies for several porous materials. Example results from these simulations are shown in Fig. 3. The exponent C_σ is obtained by least-square fitting of the simulated data to Eqn. (7). The simulation indicates that the energy dependence for different materials might be approximated with a monomial, but the exponent varies highly with the material. However, the fitted data are located roughly around $C_\sigma \approx -4$, which is used henceforth.

C. Reconstruction Framework

We propose an iterative maximum-likelihood reconstruction algorithm [25] for Talbot-Lau X-ray Computed Tomography. For beam-hardening correction, a polychromatic modeling of the imaging process is required. To additionally avoid intermittent fitting of the phase-stepping curve, it is also required to define the likelihood of the measured phase-stepping curves at each energy E from a set of attenuation, phase and scatter coefficients.

1) Forward-Projection: We assume that for a given energy, the transmission T_i, dark field D_i and object phase-shift ϕ_i seen by ray i are modeled by integration along the line-of-sight of attenuation coefficient, refractive decrement and scatter coefficient.
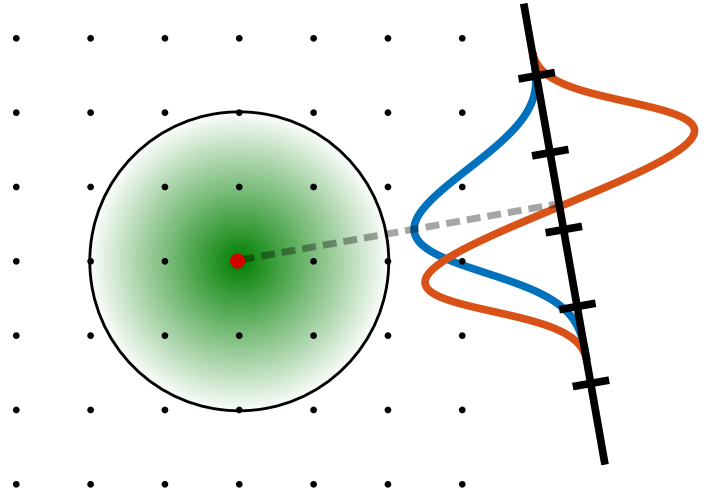
This integration could be done by an arbitrary implementation of a forward projector. However, if a standard projector is used, the differential character of the phase image would require numerical differentiation, possibly introducing numeric artifacts. Koehler *et al.* proposed to use Kaiser-Bessel functions as basis functions to phase-contrast reconstruction [29]. The main advantage is that Kaiser-Bessel functions (also known as blobs) provide analytical expressions of the Radon transform and its derivative [30].

The proposed method is implemented in parallel beam geometry, but it may be used with more complex acquisition geometries such as fan or cone beam in a straightforward manner. For the non-differential attenuation and scatter images, the weights for the system matrix elements M_{ij} are computed as the integration of the footprint of blob j over the area of detector pixel i, as shown in Fig. 4. For differential matrix elements M_{ij}^δ, integration is performed over the differential footprint.

2) Talbot-Lau Image Model: Each blob volume element j has an associated attenuation coefficient μ_j, refractive decrement δ_j and scatter coefficient σ_j. Absorption $T_i(E)$ and dark-field $D_i(E)$ seen by pixel i at energy E are given by

$$T_i(E) = \exp\left(-\sum_j M_{ij} \cdot \mu_j(E)\right) , \qquad (8)$$

and

$$D_i(E) = \exp\left(-\sum_j M_{ij} \cdot \sigma_j(E)\right) . \qquad (9)$$

The differential phase is given by

$$\Delta\phi_i(E) = \sum_j M_{ij}^\delta \cdot \delta_j(E) , \qquad (10)$$

where the differential character, usually expressed by the partial derivative $\frac{\partial}{\partial x}$ in phase stepping direction of G_2, is taken into account by the differential matrix element M_{ij}^δ.
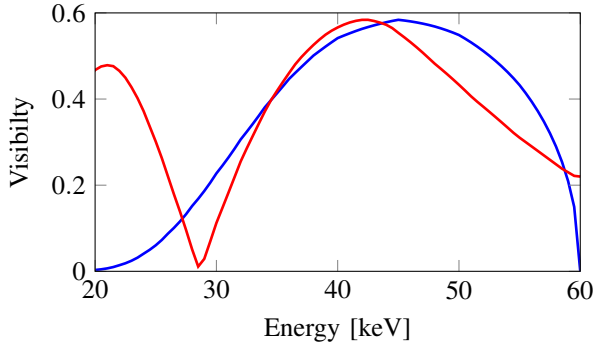
Fig. 5: Blue: X-ray spectrum scaled to arbitrary unit for better visualization. Red: Simulated visibility of the grating interferometer as a function of the photon energy.

Given the projected values $T_i(E)$, $D_i(E)$ and $\Delta\phi_i(E)$ we expect the observed photon counts $\overline{N}_{i,s}$ at stepping position s to be:

$$\overline{N}_{i,s} = \int dE \ N_i(E) \cdot (1 + V_i(E) \cdot \cos\phi_{i,s}(E)) \ , \quad (11)$$

with the expected mean photon count

$$N_i(E) = N_i^0(E) \cdot T_i(E) \ , \quad (12)$$

the expected visibility

$$V_i(E) = V_i^0(E) \cdot D_i(E), \quad (13)$$

and the expected phase

$$\phi_{i,s}(E) = \phi_i^0(E) + \phi_s + \Delta\phi_i(E) \ . \quad (14)$$

The relative phase $\phi_s := 2\pi\frac{s}{p_2}$ depends on the stepping distance s of G_2 and the grating period p_2. $N_i^0(E)$, $V_i^0(E)$, and $\phi_i^0(E)$ denote energy-dependent free-field reference measurements for pixel i. However, $N_i^0(E)$, $V_i^0(E)$, and $\phi_i^0(E)$ can not directly be measured in a setup with an energy-integrating detector. However, prior knowledge on the X-ray tube and the acquisition setup provides the per-energy amount of photons $N_i^0(E)$. Phase shift per energy $\phi_i^0(E)$ and visibility per energy $V_i^0(E)$ can be reasonably well estimated from free-field simulation using a priori knowledge the setup parameters, i.e., spectrum, source focal size, detector response and grating materials, geometry and positions. Figure 5 shows example simulations for the setup used in this paper. Here, the spectrum is plotted in blue, the energy-dependent visibility is plotted in red.

The forward model stated above is general and requires multi-spectral image data. Each voxel j is required to contain the attenuation, refractive decrement and scatter coefficient at any energy E. The information per energy is inferred from the model in Eqn. (5) to Eqn. (7). The integration over the whole spectrum is done by subdivision into an arbitrary number of energy bins and subsequent summation.

$$\overline{N}_{i,s} = \sum_k N_i(E_k \cdot (1 + V_i(E_k) \cdot \cos\phi_{i,s}(E_k)) \ . \quad (15)$$

3) Reconstruction Algorithm: For reconstruction we adapt the iterative maximum-likelihood algorithm for monochromatic Talbot-Lau tomography from [22]. Minimization of the cost function is performed by coordinate gradient descent to iteratively update attenuation, phase and scatter image [23]. In each update step a line search is done by backtracking.

Let $\theta := (\mu_j, \delta_j, \sigma_j)$ be the parameter set describing the object and $\mathbf{N} := (N_{i,s})$ the set of intensities measured by the detector. Assuming negligible electronic noise leads to the negative log-likelihood for Poisson distributed noise l,

$$l(\theta \mid \mathbf{N}) = \sum_{i,s} -N_{i,s} \cdot \ln(\overline{N}_{i,s}) + \overline{N}_{i,s} \ , \quad (16)$$

where constant terms that do not affect location of the minimum are omitted. Note that the likelihood could readily be adapted to a shifted Poisson noise model to account for electronic noise.

Derivation of Eqn. (11) with respect to each coefficient leads to the gradient

$$\frac{\partial}{\partial\mu_j}l = \sum_{i,s}(N_{i,s} - \overline{N}_{i,s}) \cdot M_{ij} \ . \quad (17)$$

$$\frac{\partial}{\partial\delta_j}l = \sum_{i,s}\left(\frac{N_{i,s}}{\overline{N}_{i,s}} - 1\right)\int dE \ N_i(E)V_i(E)\sin\phi_{i,s}(E) \cdot M_{ij}^\delta \ . \quad (18)$$

$$\frac{\partial}{\partial\sigma_j}l = \sum_{i,s}\left(\frac{N_{i,s}}{\overline{N}_{i,s}} - 1\right)\int dE \ N_i(E)V_i(E)\cos\phi_{i,s}(E) \cdot M_{ij} \ . \quad (19)$$

Implementation of the framework was done in Java using the reconstruction framework CONRAD [31]. The highest computational effort is located in the polychromatic forward-projection. This requires projection of N volumes at different energies E, where N is the number of used energy bins. Since each energy bin is mutually independent, multi-core computing was applied to reduce computation time.

III. EVALUATION & RESULTS

The evaluation in this paper is based on synthetic data affected by beam-hardening. The data were obtained using the proposed forward model with a well-defined phantom. The objective is to see if an artifact free reconstruction within the maximum-likelihood framework is possible.

For this purpose a Talbot-Lau imaging system was simulated using a wave-propagation algorithm [14]. A 60 keV tungsten tube with a source size of 300 μm is used, and a perfect detector without any cross talk is assumed. All three gratings are made of gold. The source grating G_0 has a grating period of $p_0 = 10$ μm and a height of $h_0 = 200$ μm. For the phase grating G_1, we have $p_1 = 5.716$ μm, $h_1 = 6.3$ μm. The analyzer grating G_2 has $p_2 = 10$ μm, $h_2 = 200$ μm respectively. The distance from G_0 to G_1 is 0.8 m and G_1 to G_2 is 0.6 m.

The detector consists of 300 pixels with a size of 333 μm each. The reconstructed volume is 256^2 with a voxel size of
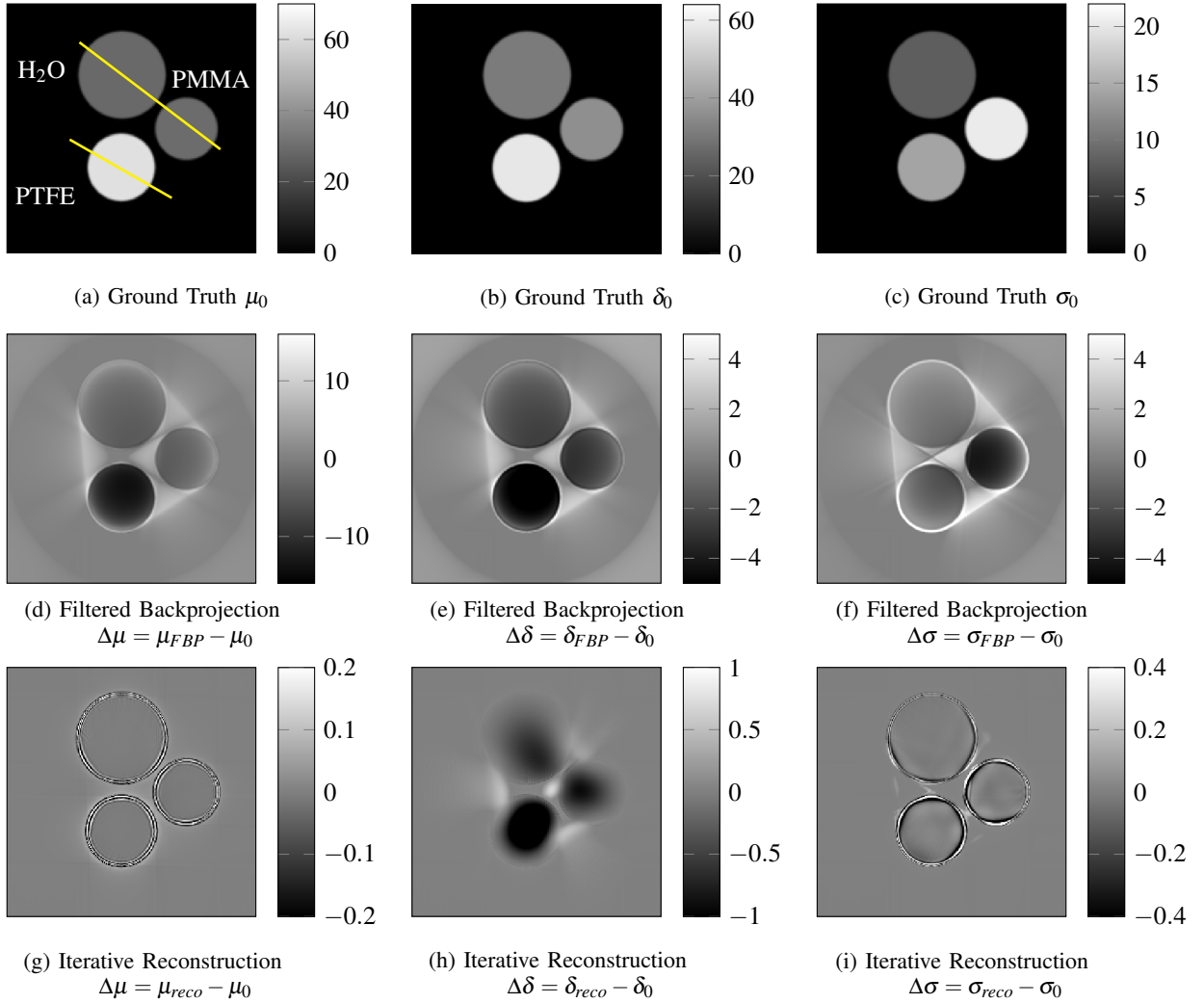
Fig. 6: The first row shows ground truth data for absorption, refractive decrement and scatter at a mean energy of $E_0 = 38.8\,\mathrm{keV}$. The two yellow lines define crosssections shown in Fig. 7. The range of the refractive decrement δ was scaled to be in the same range as the attenuation coefficient by multiplication of 0.2×10^8. The second row shows the difference between the direct reconstruction using filtered backprojection and ground truth data. The third row shows the difference between the iterative reconstruction and ground truth data. The error of the iterative reconstruction is a magnitude smaller than for the filtered backprojection reconstruction.

390 µm. The angular range is 2π with 480 projection images using a parallel beam setup where three phase steps per projection angle are performed. The mean reference photon count is constant over the detector with $N_{tot}^0 = 4.5 \times 10^6$ photons detected by each pixel per exposure. The spectrum was binned into 15 energy bins.

A numerical phantom is defined consisting of three cylinders of different material each, see Fig. 6. The largest cylinder is filled with H_2O and has radius of $17.5\,\mathrm{mm}$. The second cylinder has a radius of $13.5\,\mathrm{mm}$ and is filled with PTFE. The smallest has a radius of $12.5\,\mathrm{mm}$ and contains PMMA. The attenuation coefficient μ and refractive decrement δ are taken from tabulated values [32].

The dark-field signal is a special case in the phantom. An entirely homogeneous cylinder would not create any dark-field, leading to a scatter coefficient σ of 0. Instead, we assume that each cylinder is filled with numerous micrometer-sized objects. Such small components, modeling for example sandy or spongy material, create significant dark-field due to small angle scattering [33]. Uniformly distributed small components are expected to lead to a constant scatter coefficient across each cylinder. For our synthetic phantom, we choose $\sigma(\mathrm{PMMA}) = 20$, $\sigma(\mathrm{PTFE}) = 14$, and $\sigma(H_2O) = 8$ at a mean energy $E_0 = 38.8\,\mathrm{keV}$. Synthetic phase-stepping data of the phantom are generated with the proposed forward model using the setup parameter from above.

Next, phase-retrieval is performed via least-square fitting on the phase-stepping data. Subsequently, the obtained attenuation, phase and dark-field sinograms are reconstructed using filtered back projection. We use the Ram-Lak filter for
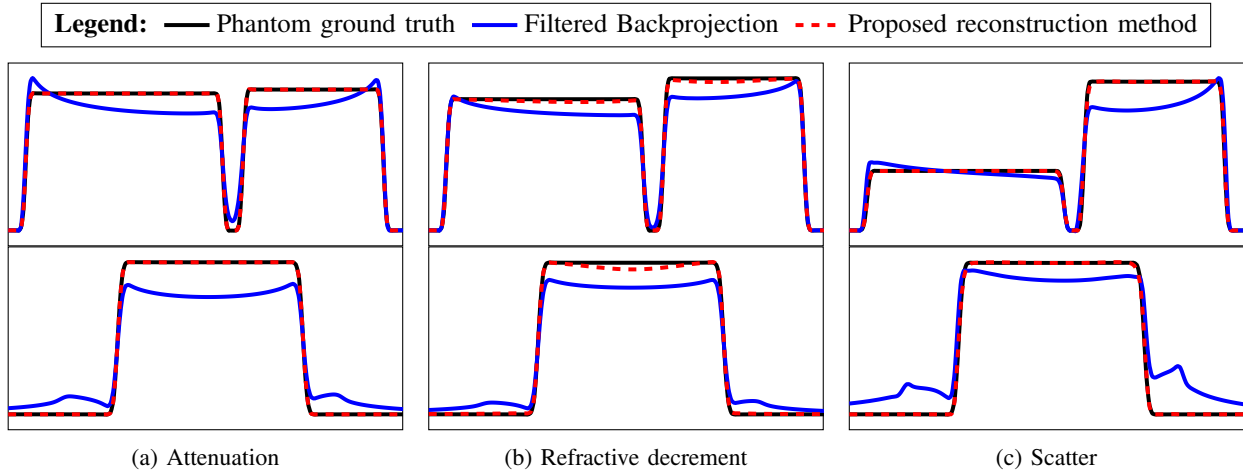
Fig. 7: Two cross-sections through the reconstructed data as visualized in Fig. 6. Black: Phantom ground truth, Blue: Filtered Backprojection, Red (dashed): Proposed reconstruction method. For all images, the iteratively reconstruction and ground truth are in high agreement.

attenuation and scatter, and the Hilbert filter for the differential phase image. This reconstruction is used as an initial solution for the proposed reconstruction algorithm. The algorithm is stopped after 200 iterations.

Figure 6 shows the difference between ground truth and the reconstruction results. From left to right, the images show distributions of absorption, phase, and scatter. In the top row, the ground truth is shown. The second and third row show the result of filtered backprojection and of the proposed algorithm. The two lines in Fig. 6 (a) indicate the location of the associated cross-section lineplots that are shown in Fig. 7. Here, ground truth is shown in black, the result by filtered backprojection is shown in blue, and the proposed method is shown by the red dashed line. In all three images reconstructed with filtered backprojection, typical cupping and streak artifacts are visible. These artifacts are more pronounced in attenuation and scatter than in the phase image. This is because the refractive decrement decays with only E^{-2}, while attenuation and scatter yield a stronger energy dependence.

The proposed algorithm is able to reconstruct all three images with almost all polychromatic artifacts removed. Reconstruction of attenuation and scatter are almost perfect. The phase-image exhibits slight cupping artifacts. We assume that these artifacts might also disappear if a higher number of iterations were chosen, but we will investigate this in greater detail in future work. Overall, we observed that attenuation and scatter images converge much faster than the phase-images. A similar behavior has already been mentioned by Brendel *et al.* with a maximum-likelihood reconstruction for monochromatic Talbot-Lau imaging [23]. We assume that this behavior originates from the differential nature of the phase image and the non-convexity of the cost function.

IV. CONCLUSION

We propose a new reconstruction algorithm that incorporates a polychromatic model in grating based phase-contrast imaging. The biggest benefit of polychromatic modeling is that it implicitly avoids beam-hardening artifacts. To our knowledge, this is the first tomographic reconstruction algorithm that is specifically designed for polychromatic Talbot-Lau imaging.

For synthetic phantom data, the proposed method is able to correct beam-hardened corrupted data for reconstructions of attenuation, phase and scatter. Results for attenuation and scatter are highly accurate. The phase image is also greatly improved over a naive reconstruction, but still exhibits slight cupping artifacts. Also, we observed that reconstruction of attenuation and scatter converges much faster than reconstruction of the phase. We believe that the slow convergence can be efficiently targeted with a specially tailored optimization algorithm.

In future work, we will evaluate the algorithm on real data such as well-defined physical phantoms and medical data. Another important aspect will be to compare the presented method to state-of-the-art beam hardening corrections.

REFERENCES

[1] A. Momose, T. Takeda, Y. Itai, and K. Hirano, "Phase–contrast x–ray computed tomography for observing biological soft tissues," *Nature Medicine*, vol. 2, pp. 473–475, Apr. 1996.

[2] S. W. Wilkins, T. E. Gureyev, D. Gao, A. Pogany, and A. W. Stevenson, "Phase-contrast imaging using polychromatic hard x-rays," *Nature*, vol. 384, pp. 335–338, Nov. 1996.

[3] S.-A. Zhou and A. Brahme, "Development of phase-contrast x-ray imaging techniques and potential medical applications," *Physica Medica*, vol. 24, pp. 129–148, Sep. 2008.

[4] T. Donath, F. Pfeiffer, O. Bunk, C. Grünzweig, E. Hempel, S. Popescu, P. Vock, and C. David, "Toward clinical x-ray phase-contrast CT," *Investigative Radiology*, p. 1, May 2010.

[5] G. Schulz, T. Weitkamp, I. Zanette, F. Pfeiffer, F. Beckmann, C. David, S. Rutishauser, E. Reznikova, and B. Muller, "High-resolution tomographic imaging of a human cerebellum: comparison of absorption and grating-based phase contrast," *Journal of The Royal Society Interface*, vol. 7, pp. 1665–1676, July 2010.

[6] M. Bech, O. Bunk, T. Donath, R. Feidenhans'l, C. David, and F. Pfeiffer, "Quantitative x-ray dark-field computed tomography," *Physics in Medicine and Biology*, vol. 55, pp. 5529–5539, Aug. 2010.

[7] A. Velroyen, A. Yaroshenko, D. Hahn, A. Fehringer, A. Tapfer, M. Mueller, P. Noel, B. Pauwels, A. Sasov, A. Yildirim, O. Eickelberg, K. Hellbach, S. Auweter, F. Meinel, M. Reiser, M. Bech, and F. Pfeiffer, "Grating-based x-ray dark-field computed tomography of living mice," *EBioMedicine*, vol. 2, pp. 1500–1506, Oct. 2015.

[8] T. Michel, J. Rieger, G. Anton, F. Bayer, M. W. Beckmann, J. Durst, P. A. Fasching, W. Haas, A. Hartmann, G. Pelzer, M. Radicke, C. Rauh, A. Ritter, P. Sievers, R. Schulz-Wendtland, M. Uder, D. L. Wachter, T. Weber, E. Wenkel, and A. Zang, "On a dark-field signal generated by micrometer-sized calcifications in phase-contrast mammography," *Physics in Medicine and Biology*, vol. 58, pp. 2713–2732, Apr. 2013.

[9] Z. Wang, N. Hauser, G. Singer, M. Trippel, R. A. Kubik-Huch, C. W. Schneider, and M. Stampanoni, "Non-invasive classification of microcalcifications with phase-contrast x-ray mammography," *Nature Communications*, vol. 5, May 2014.

[10] F. Pfeiffer, T. Weitkamp, O. Bunk, and C. David, "Phase retrieval and differential phase-contrast imaging with low-brilliance x-ray sources," *Nature Physics*, vol. 2, pp. 258–261, March 2006.

[11] P. Thibault, M. Dierolf, A. Menzel, O. Bunk, C. David, and F. Pfeiffer, "High-resolution scanning x-ray diffraction microscopy," *Science*, vol. 321, pp. 379–382, July 2008.

[12] N. Bevins, J. Zambelli, K. Li, Z. Qi, and G.-H. Chen, "Beam hardening in x-ray differential phase contrast computed tomography," in *Medical Imaging 2011: Physics of Medical Imaging* (N. J. Pelc, E. Samei, and R. M. Nishikawa, eds.), SPIE-Intl Soc Optical Eng, March 2011.

[13] M. Chabior, T. Donath, C. David, O. Bunk, M. Schuster, C. Schroer, and F. Pfeiffer, "Beam hardening effects in grating-based x-ray phase-contrast imaging," *Medical Physics*, vol. 38, p. 1189, Feb. 2011.

[14] G. Pelzer, G. Anton, F. Horn, J. Rieger, A. Ritter, J. Wandner, T. Weber, and T. Michel, "A beam hardening and dispersion correction for x-ray dark-field radiography," *Medical Physics*, vol. 43, pp. 2774–2779, May 2016.

[15] W. Yashiro, P. Vagovič, and A. Momose, "Effect of beam hardening on a visibility-contrast image obtained by x-ray grating interferometry," *Optics Express*, vol. 23, p. 23462, Aug. 2015.

[16] G. T. Herman, "Correction for beam hardening in computed tomography," *Physics in Medicine and Biology*, vol. 24, pp. 81–106, Jan. 1979.

[17] J. F. Barrett and N. Keatba, "Artifacts in CT: Recognition and avoidance," *RadioGraphics*, vol. 24, pp. 1679–1691, Nov. 2004.

[18] B. D. Man, J. Nuyts, P. Dupont, G. Marchal, and P. Suetens, "An iterative maximum-likelihood polychromatic algorithm for CT," *IEEE Transactions on Medical Imaging*, vol. 20, pp. 999–1008, Oct. 2001.

[19] S. Kaeppler, F. Bayer, T. Weber, A. Maier, G. Anton, J. Hornegger, M. Beckmann, P. A. Fasching, A. Hartmann, F. Heindl, T. Michel, G. Oezguel, G. Pelzer, C. Rauh, J. Rieger, R. Schulz-Wendtland, M. Uder, D. Wachter, E. Wenkel, and C. Riess, "Signal decomposition for x-ray dark-field imaging," in *Medical Image Computing and Computer-Assisted Intervention – MICCAI 2014*, pp. 170–177, Springer Nature, Sep. 2014.

[20] A. C. Kak and M. Slaney, *Principles of Computerized Tomographic Imaging*. Society for Industrial & Applied Mathematics (SIAM), Jan. 2001.

[21] T. Koehler and B. Brendel, "Empirical beam hardening correction for differential phase contrast ct," Aug. 25 2016. US Patent App. 15/031,819.

[22] A. Ritter, F. Bayer, J. Durst, K. Gödel, W. Haas, T. Michel, J. Rieger, T. Weber, L. Wucherer, and G. Anton, "Simultaneous maximum-likelihood reconstruction for x-ray grating based phase-contrast tomography avoiding intermediate phase retrieval," *arXiv preprint arXiv:1307.7912*, Jul. 2013.

[23] B. Brendel, M. von Teuffenbach, P. B. Noël, F. Pfeiffer, and T. Koehler, "Penalized maximum likelihood reconstruction for x-ray differential phase-contrast tomography," *Medical Physics*, vol. 43, pp. 188–194, Dec. 2015.

[24] A. Ritter, G. Anton, and T. Weber, "Simultaneous maximum-likelihood reconstruction of absorption coefficient, refractive index and dark-field scattering coefficient in x-ray talbot-lau tomography," *PLOS ONE*, vol. 11, p. e0163016, Oct. 2016.

[25] I. Elbakri and J. Fessler, "Statistical image reconstruction for polyenergetic x-ray computed tomography," *IEEE Transactions on Medical Imaging*, vol. 21, pp. 89–99, Feb. 2002.

[26] A. Lohmann and D. Silva, "An interferometer based on the talbot effect," *Optics Communications*, vol. 2, pp. 413–415, Feb. 1971.

[27] M. Chabior, *Contributions to the characterization of grating-based x-ray phase-contrast imaging*. PhD thesis, TU Dresden, Sep. 2011.

[28] A. Ritter, P. Bartl, F. Bayer, K. C. Gödel, W. Haas, T. Michel, G. Pelzer, J. Rieger, T. Weber, A. Zang, and G. Anton, "Simulation framework for coherent and incoherent x-ray imaging and its application in talbot-lau dark-field imaging," *Optics Express*, vol. 22, p. 23276, Sep. 2014.

[29] T. Koehler, B. Brendel, and E. Roessl, "Iterative reconstruction for differential phase contrast imaging using spherically symmetric basis functions," *Medical Physics*, vol. 38, p. 4542, July 2011.

[30] R. M. Lewitt, "Multidimensional digital image representations using generalized kaiser–bessel window functions," *Journal of the Optical Society of America A*, vol. 7, p. 1834, Oct. 1990.

[31] A. Maier, H. G. Hofmann, M. Berger, P. Fischer, C. Schwemmer, H. Wu, K. Mueller, J. Hornegger, J.-H. Choi, C. Riess, A. Keil, and R. Fahrig, "A software framework for cone-beam imaging in radiology," *Medical Physics*, vol. 40, p. 111914, Nov. 2013.

[32] M. Berger and J. Hubbell, "XCOM: Photon cross sections on a personal computer," tech. rep., July 1987.

[33] W. Yashiro, Y. Terui, K. Kawabata, and A. Momose, "On the origin of visibility contrast in x-ray talbot interferometry," *Optics Express*, vol. 18, pp. 16890–16901, July 2010.